Revealing dipolar coupling with NQR off-resonant pulsed spin locking

M. W. Malone, M. McGillvray, and K. L. Sauer*
George Mason University, Fairfax, Virginia 22030, USA
(Received 10 August 2011; published 21 December 2011)

Unexpectedly, we observe a strong Gaussian decay in the nuclear quadrupole resonance signal obtained from a powder sample of spin-1 nuclei under perturbation by off-resonant radio frequency pulses. Using a model composed of just pairs of nuclei, we theoretically determine that the decay is due to the homonuclear dipolar coupling being selectively unrefocused by the pulses. We find that the decay rate measures the dipolar coupling's strength and permits us to determine how much of the sample's linewidth is due to homonuclear dipolar coupling versus electric-field gradient inhomogeneity. Furthermore, knowing the strength, shape, frequency, and timing of the pulses that lead to this rapid decay is critical for the purposes of illicit substance detection since it reduces the signal and can lead to a false negative. We find that the experimental parameters that lead to this Gaussian decay are explained well by this simple model, which leads to a method for suppressing or revealing the decay. We confirm our theoretical understanding using two samples of sodium nitrite that vary in their broadening due to electric-field gradient inhomogeneity by as much as a factor of 3.

DOI: 10.1103/PhysRevB.84.214430 PACS number(s): 76.60.Gv, 82.56.Jn, 76.60.Lz, 33.15.−e

I. INTRODUCTION

Nuclear quadrupole resonance (NQR) spectroscopy is a promising approach for the detection of quadrupole nuclei within crystalline and semicrystalline samples since it can be performed without the complexity of static external electric or magnetic fields. Useful for relatively low cost and simple substance detection, e.g., the detection of explosives and narcotics, NQR is constrained by its characteristically low frequencies and correspondingly weak signals. One way of compensating for this poor sensitivity is to apply not just a single radio-frequency (rf) excitation pulse but a rapid series of such pulses in order to lock the signal in time.[1–5] The idea behind this pulsed spin locking is to continually refocus the decoherence caused by the various line-broadening mechanisms. Pulsed spin locking was applied to NQR by Marino and Klainer[6] in the form known as a spin-locked spin-echo (SLSE) sequence, following the initial successful application of this sequence to nuclear magnetic resonance (NMR).[7] A SLSE begins with an excitation pulse θ_0 to create the initial signal, followed by a series of refocusing pulses θ, shifted in phase by 90° from the first pulse, which serve to continually rephase the signal. The sequence is written, for N refocusing pulses, as $\theta_{0x} - (\tau - \theta_y - \tau)_N$, where 2τ is the time between the refocusing pulses. The NQR signal peaks at a time τ after each refocusing pulse to create an echo train whose behavior varies due to the timing, rf, strength, and shape of the refocusing pulses, as well as the broadening mechanisms responsible for the sample's natural linewidth. The dominant broadening mechanisms are assumed to be homonuclear dipolar coupling and electric-field gradient (EFG) inhomogeneity; the second-order broadening effect of heteronuclear dipolar coupling,[8] which can be significant for organic compounds, is neglected.

Previous analyses of the signal's decay focus on its exponential behavior.[6,9,10] However, we unexpectedly found that, under certain off-resonant conditions, the signal detected with a SLSE sequence for a powder of spin-1 nuclei begins with a strong fast Gaussian decay. The conditions under which this decay appears, as well as its initial intensity, are explained well with the theoretical argument presented in Sec. II. The decay is due to the homonuclear dipolar coupling not being rephased by the refocusing pulses, while EFG inhomogeneity is rephased. This causes the envelope of the echo train to behave as though the signal decay was due entirely to the unrefocused dipolar coupling, an observation similar to that observed in NMR.[11–13] Therefore, the width of this Gaussian component in time is a measurement of the dipolar coupling of the sample. To observe the homonuclear dipolar coupling in NMR requires pulses that give a nutation angle exactly equal to π or complicated excitation sequences to simulate the same. In NQR, however, the effective nutation angle of a pulse depends on the orientation of an individual crystallite with respect to the direction of the applied rf pulse and, therefore, is not at all homogeneous across the sample. It is not surprising, therefore, that although the NMR experiments revealing homonuclear dipolar coupling are performed with resonant pulses, the same resonant experiment in NQR does not reveal a similar result. However, we find, for certain off-resonant pulses, that the combined nutation angle of the pulse and off-resonance evolution does give an effective π pulse over the sample. These conditions allow a robust and direct measurement of homonuclear dipolar coupling in a powder sample at zero field.

The ability to measure the homonuclear dipolar coupling is very valuable for substance detection since its relative contribution to the linewidth determines the off-resonant behavior of the signal as discussed in Sec. IV. Due to temperature variations of the target substance, the NQR resonance frequencies may only be known to within a certain range. Therefore, knowing the behavior of the signal as a function of off-resonance allows for the optimization of the detection sequence to ensure working in a region of strong signal for the target substance.

II. THEORY

Building upon a previous framework,[14,15] a theoretical derivation of the signal detected from spin-1 nuclei due to the time-varying SLSE Hamiltonian is given by examining

the evolution of the density matrix for a system composed of two such nuclei: spin a and spin b. Neglecting the degenerate case, there are three eigenenergies corresponding to the three eigenstates ($|x\rangle$,$|y\rangle$,$|z\rangle$) of the quadrupole Hamiltonian H_Q for a single spin-1 nucleus. Using the $\hat{x},\hat{y},\hat{z}$ coordinate axes defined by the principal axes frame (PAF) of the EFG at the nucleus,[16] with $|V_{zz}| > |V_{yy}| > |V_{xx}|$, these eigenstates correspond to the axis of symmetry of the distribution of the nucleus's protons. This is shown by calculating the expectation value, when in an eigenstate of the quadrupole Hamiltonian, of the quadrupole operator $Q^{(op)}_{x_i x_i} \propto 3x_i x_i - r^2$, which measures the deviation of the charge distribution from a sphere[17] about each axis x_i. For example, because $\langle x|Q^{(op)}_{yy}|x\rangle = \langle x|Q^{(op)}_{zz}|x\rangle = -\frac{1}{2}\langle x|Q^{(op)}_{xx}|x\rangle$ and the off-diagonal terms are zero, the proton distribution must be symmetric about the $\hat{x}$ axis since the distributions about $\hat{y}$ and $\hat{z}$ are equal. Similar results can be derived for $|y\rangle$ and $|z\rangle$.

For the two-spin model, there are nine permutations of the system's eigenstate $|ab\rangle$, shown in Fig. 1, where a is the quadrupole eigenstate of spin a and likewise for b. The quadrupole Hamiltonian can be expressed as

$$\begin{aligned} H_Q = {} & 2\epsilon_z|1\rangle\langle 1| + (\epsilon_z+\epsilon_x)(|2\rangle\langle 2| + |3\rangle\langle 3|) + 2\epsilon_x|4\rangle\langle 4| \\ & +(\epsilon_z+\epsilon_y)(|5\rangle\langle 5| + |6\rangle\langle 6|) + (\epsilon_x+\epsilon_y)(|7\rangle\langle 7| \\ & +|8\rangle\langle 8|) + 2\epsilon_y|9\rangle\langle 9|, \end{aligned} \tag{1}$$

with $\epsilon_y \equiv [V_{zz}+(V_{xx}-V_{yy})]\frac{eQ}{4}$, $\epsilon_x \equiv [V_{zz}-(V_{xx}-V_{yy})]\frac{eQ}{4}$, $\epsilon_z \equiv -\epsilon_x - \epsilon_y$, and Q is the nuclear quadrupole moment. For simplicity, we assume the PAFs of the two spins are aligned with each other.

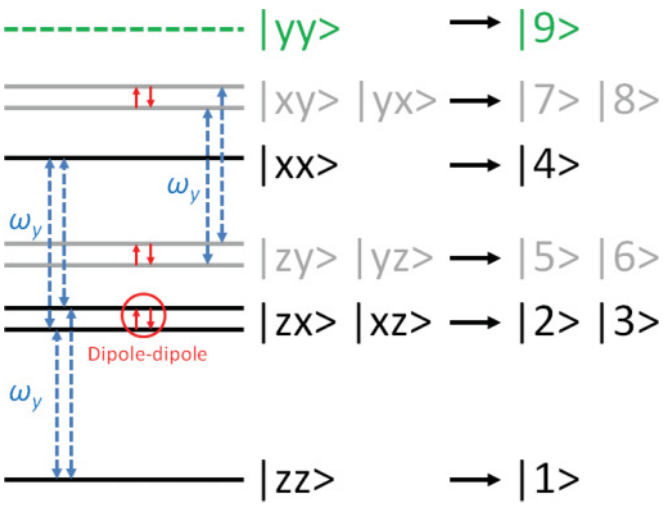

FIG. 1. (Color online) The eigenenergies are shown for spin a and spin b where $|x\rangle$,$|y\rangle$,$|z\rangle$ correspond to the eigenstates of the quadrupole Hamiltonian. The allowed transitions due to the rf Hamiltonian under the secular approximation in the interaction representation are given for $\omega_{rf} = \omega_y$. Similarly, the transitions allowed by the dipolar coupling are highlighted by separating the degenerate states. No transitions between the sets of gray and black levels, the V and W levels, respectively, are possible under these assumptions. Additionally, no transitions involving the single green level are possible.

Perturbations from the dipolar coupling H_d and rf H_{rf} Hamiltonians during the SLSE sequence will govern the transitions between levels. H_d is expressed as

$$H_d = \frac{\mu_0}{4\pi}\frac{\gamma^2\hbar^2}{r^3}[\mathbf{I}_a\cdot\mathbf{I}_b - 3(\mathbf{I}_a\cdot\hat{r})(\mathbf{I}_b\cdot\hat{r})], \tag{2}$$

where μ_0 is the permeability of free space, γ is the gyromagnetic ratio of the nucleus, $\mathbf{r} = r\hat{r}$ is the displacement vector of the two nuclei, $\mathbf{I}_a$ is the angular momentum operator for spin a with magnetic moment $\vec{\mu} = \gamma\hbar\mathbf{I}_a$ and similarly for spin b. H_{rf} for a pulse of magnitude B, direction $\hat{B}$, and phase ϕ is given by

$$H_{rf} = -\gamma\hbar\,\cos(\omega_{rf}t - \phi)[\mathbf{B}\cdot(\mathbf{I}_a + \mathbf{I}_b)], \tag{3}$$

where we assume ω_{rf} is close to $\omega_y \equiv \frac{\epsilon_z-\epsilon_x}{\hbar}$. While we have singled out one of the three characteristic NQR frequencies for specificity, the conclusions are extended easily to the other frequencies.

The total Hamiltonian H_{total} governs the time evolution of the density matrix $\varrho(t)$ by the Liouville equation,

$$\dot{\varrho} = \frac{i}{\hbar}[\varrho, H_{\text{total}}], \tag{4}$$

where H_{total} can be rewritten as

$$H_{\text{total}} = H_0 + U + H_{rf} + H_d. \tag{5}$$

Note that the quadrupole Hamiltonian has been split into two components $H_Q = H_0 + U$ with $H_0 \equiv \frac{\omega_{rf}}{\omega_y}H_Q$, $U \equiv -\frac{\Delta\omega}{\omega_y}H_Q$, and $\Delta\omega \equiv \omega_{rf} - \omega_y = 2\pi\,\Delta f$. This will simplify the derivation by removing the time dependency of H_{rf} in the interaction representation of the dominant Hamiltonian H_0. We add that the dominant effect of the EFG inhomogeneity is to create a distribution in the operator U among pairs of nuclei.

Entering the interaction representation of H_0, Eq. (4) becomes

$$\dot{\tilde{\varrho}} = \frac{i}{\hbar}[\tilde{\varrho}, U + \tilde{H}_{rf} + \tilde{H}_d], \tag{6}$$

where the interaction representation of the density matrix $\tilde{\varrho} \equiv e^{(i/\hbar)H_0t}\varrho e^{(-i/\hbar)H_0t}$ and $\tilde{H} \equiv e^{(i/\hbar)H_0t}He^{(-i/\hbar)H_0t}$. As shown in Fig. 1, transitions are only possible within two sets of four levels, the W and V levels, under the secular approximation. Since the set of W levels does not interact with the set of V levels, only 4×4 matrices are needed to represent the action of an operator on each set of levels. Working in the fictitious spin-1/2 space $(\hat{i},\hat{j},\hat{k})$, Dirac matrices are used to rewrite H_{rf} and H_Q, shown in Table I, because of their convenient commutation relationships. With this notation, H_Q becomes

$$H_Q = \hbar\omega_y\left(I_3^W + I_3^V\right) + \frac{\epsilon_y}{2}(4|9\rangle\langle 9| + \mathbf{1}^W + \mathbf{1}^V), \tag{7}$$

with a similar expression for $\tilde{U} = U$. Recognizing $I_y = I_{ya} + I_{yb} = 2(I_2^V + I_2^W)$, and under the secular approximation, it can be shown that $\tilde{H}_{rf}$ is time independent,[15]

$$\tilde{H}_{rf} = -\gamma\hbar B\,\cos\,\psi\left(\cos\,\phi\left[I_2^W + I_2^V\right] + \sin\,\phi\left[I_1^W + I_1^V\right]\right). \tag{8}$$

Here, the $\cos\,\psi \equiv \hat{B}\cdot\hat{y}$ term is the reduction in the effective strength of the rf due to its random orientation with the y axis

TABLE I. The relationship between H_{rf} and H_Q suggests the definition of two fictitious spin-1/2 angular momentum operators $\mathbf{I}^W = (I_1^W\hat{i}, I_2^W\hat{j}, I_3^W\hat{k})$ and $\mathbf{I}^V = (I_1^V\hat{i}, I_2^V\hat{j}, I_3^V\hat{k})$, which are expressed in terms of the Dirac matrices.[18] The superscripts indicate the set of levels the operator acts on, e.g., $I_1^W = \sum_{p=1}^{4}\sum_{q=1}^{4}[\rho_1(p,q) + \sigma_1(p,q)]|p\rangle\langle q|$ and $I_1^V = \sum_{p=5}^{8}\sum_{q=5}^{8}[\rho_1(p-4,q-4) + \sigma_1(p-4,q-4)]|p\rangle\langle q|$.

	I_1^i	I_2^i	I_3^i
$\mathbf{I}^W \equiv$	$(\rho_1 + \sigma_1)/2$	$(\rho_2 + \sigma_2)/2$	$(\rho_3 + \sigma_3)/2$
$\mathbf{I}^V \equiv$	$\rho_1/2$	$\rho_2/2$	$\rho_3/2$

of the PAF of the nucleus's EFG: a consequence of a powder sample. For an excitation pulse with phase ϕ_0, the refocusing pulses will have a phase $\phi = \phi_0 \pm \frac{\pi}{2}$ in order to lock the signal created by the excitation pulse.

$\tilde{H}_d$ under the secular approximation can be expressed as

$$\tilde{H}_d/\hbar \approx \alpha_y(|2\rangle\langle 3| + |3\rangle\langle 2|) + \alpha_x(|5\rangle\langle 6| + |6\rangle\langle 5|) + \alpha_z(|7\rangle\langle 8| + |8\rangle\langle 7|), \quad (9)$$

with the coefficients given as $\alpha_y = \frac{\mu_0}{4\pi}\frac{\gamma^2\hbar}{r^3}[1 - 3(\hat{y}\cdot\hat{r})^2]$ and similarly for α_x, α_z. While $\tilde{H}_d$ can also be written in terms of Dirac matrices, it is not illuminating to the discussion. In its present form, however, it is easy to see both the flip-flop terms that drive the interaction and that $\tilde{H}_d$ commutes with H_Q and U.

The SLSE begins with an excitation pulse, assumed for simplicity to be a δ-function pulse, to create the initial signal and is followed by a string of refocusing pulses. During the delays of duration τ between pulses, $\tilde{H}_{\text{total}}$ consists of just $\tilde{H}_d$ and U. During a pulse, it is assumed that $\tilde{H}_{rf}$ is so much greater than $\tilde{H}_d$ that the dipolar coupling's contribution can be dropped and $\tilde{H}_{\text{total}} \approx \tilde{H}_{rf} + U$. As confirmation of the validity of this approximation for our experiments, we also numerically solved for the evolution of the signal incorporating the dipolar coupling during the pulse and found that the two results were indistinguishable within computational error. Recognizing that $\tilde{H}_{rf}$ and $\tilde{H}_d$ are independent of time under the secular approximation, the evolution of $\tilde{\varrho}$, after N refocusing pulses of length t_p, is

$$\tilde{\varrho}(t = 2N\tau + t_pN) = (DPD)^N\tilde{\varrho}(t = 0^+)(DPD)^{\dagger N}. \quad (10)$$

Here, we distinguish evolution due to the dipolar coupling,

$$D \equiv e^{(-i/\hbar)\tilde{H}_d\tau}, \quad (11)$$

from evolution due to the pulse and the free evolution,

$$P \equiv e^{(-i/\hbar)U\tau}e^{(-i/\hbar)(\tilde{H}_{rf}+U)t_p}e^{(-i/\hbar)U\tau}, \quad (12)$$

and define $\varrho(t = 0^+)$ as the density matrix after the excitation pulse.

The initial density matrix is found using the equipartition theorem in the high-temperature limit $\varrho_0 = \frac{1}{9}(\mathbf{1}^W + \mathbf{1}^V + |9\rangle\langle 9| - \frac{H_Q}{kT})$. The behavior of the magnetic moments in the laboratory frame produces the signal given by

$$\langle I_y\rangle = \text{Tr}[\varrho I_y] = \text{Tr}[\tilde{\varrho}\tilde{I}_y], \quad (13)$$

with

$$\tilde{I}_y = 2\left(I_2^V + I_2^W\right)\cos\omega_{rf}t + 2\left(I_1^V + I_1^W\right)\sin\omega_{rf}t. \quad (14)$$

Since the identity matrices and the $|9\rangle\langle 9|$ term commute with P and D and since their trace with $\mathbf{I}^V$ and $\mathbf{I}^W$ is zero, those terms can be ignored in ϱ_0. By a similar argument, they can also be dropped from U. This allows ϱ_0 to be reduced to

$$\varrho_0 = -\frac{\hbar\omega_y}{9kT}\left(I_3^W + I_3^V\right). \quad (15)$$

After the initial pulse of duration t_{p0} and phase ϕ_0, the density matrix becomes[15]

$$\varrho(t = 0^+) = \tilde{\varrho}(t = 0^+) = \frac{\hbar\omega_y}{9kT}\sin\theta_0'(\mathbf{I}^W + \mathbf{I}^V)\cdot\hat{i}, \quad (16)$$

where the nutation angle $\theta_0 = \gamma Bt_{p0}$ is reduced by the directional cosine to give the effective nutation angle for a given crystallite $\theta_0' = \theta_0\cos\psi$. Experimentally, we choose $\theta_0 = 2.077$ since it provides the greatest signal for a powder.[19] The components of $\mathbf{I}^W$ and $\mathbf{I}^V$ in the $\hat{k}$ direction have been dropped from $\varrho(t = 0^+)$ since we subtract subsequent experiments with $\phi_0 = 0$ and $\phi_0 = \pi$ to eliminate any signals that might arise from either the $\hat{k}$ component or probe ringing due to the refocusing pulses.

While Eqs. (10) and (16) give the complete solution to the evolution of the signal, it is instructive to look for symmetries in the solution, particularly with regard to the frequency and strength of the refocusing pulse. We, therefore, turn to examine the operator P of Eq. (12) more closely to note that the relevant operators within it consist exclusively of the fictitious spin-1/2 operators given in Table I. This allows P to be treated as the sum of three rotations where the first and the third rotations are determined by off-resonance alone and the middle or second rotation by the effects of the refocusing pulse and the off-resonance condition. The refocusing pulse is characterized by the nutation angle $\theta = \gamma Bt_p$, which for a given crystallite is reduced by the directional cosine to give the effective nutation angle $\theta' = \theta\cos\psi$. Therefore, we can write the three rotations as $\theta_1\hat{n}_1 = \theta_3\hat{n}_3 = 2\pi\,\Delta f\,\tau\hat{k}$ for the delays of duration τ; and $\theta_2\hat{n}_2 = \theta'\hat{i} + \theta_1\frac{t_p}{\tau}\hat{k}$ ($\phi = \frac{\pi}{2}$) during the pulse. For a given crystallite orientation, the net rotation $\theta_{\text{tot}}\hat{n}_{\text{tot}}$ is the same for both the W and the V levels and can be found using quaternions. P becomes

$$P = e^{i\theta_{\text{tot}}\mathbf{I}^W\cdot\hat{n}_{\text{tot}}}e^{i\theta_{\text{tot}}\mathbf{I}^V\cdot\hat{n}_{\text{tot}}}, \quad (17)$$

where

$$\cos\frac{\theta_{\text{tot}}}{2} = \cos\theta_1\cos\frac{\theta_2}{2} - \sin\theta_1\sin\frac{\theta_2}{2}\hat{n}_1\cdot\hat{n}_2, \quad (18)$$

and

$$\sin\frac{\theta_{\text{tot}}}{2}\hat{n}_{\text{tot}} = \sin\frac{\theta_2}{2}\hat{n}_2 + \sin\theta_1\cos\frac{\theta_2}{2}\hat{n}_1 + (\cos\theta_1 - 1)\sin\frac{\theta_2}{2}\hat{n}_1(\hat{n}_1\cdot\hat{n}_2). \quad (19)$$

The operator P is clearly periodic in θ_1 and $\frac{\theta_2}{2}$, so the signal will be periodic in these as well. In the limit of δ-function

pulses, where $\hat{n}_1 \cdot \hat{n}_2 = 0$ and $\hat{n}_2 = \hat{i}$, $\theta_{\rm tot}$ is insensitive to the sign of the off-resonance, while the $\hat{k}$ component of $\hat{n}_{\rm tot}$ flips sign. Due to both the phase cycling of the pulse sequence and the idealized pulse shape, this flip will not impact the signal, which will be symmetrical as a function of off-resonance. In the same δ-function limit, an increase in θ_1 by π should produce the same signal, so the signal repeats off-resonance with a period of $\frac{1}{2\tau}$, which is a periodicity seen for various sequences.[9,10,15,20] Within this periodicity, we observe extremes in the signal behavior at $\Delta f = \frac{m}{2\tau}$, for integer m, corresponding to $\theta_{\rm tot}\hat{n}_{\rm tot} = \theta_2\hat{i}$ and at $\Delta f = \frac{1}{4\tau} + \frac{m}{2\tau}$, corresponding to $\theta_{\rm tot}\hat{n}_{\rm tot} = \pi(\sin\frac{\theta_2}{2}\hat{i} + \cos\frac{\theta_2}{2}\hat{k})$. Note that, if $\theta_2 = \pi$, then $\hat{n}_{\rm tot} = \hat{i}$, regardless of Δf. This means $\tilde{\varrho}$, starting from Eq. (16), is locked along $\hat{i}$, making the evolution due to EFG inhomogeneity refocus under this condition. However, for $\theta_2 = \frac{\pi}{2}$, $\theta_{\rm tot}\hat{n}_{\rm tot}$ varies from $\frac{\pi}{2}\hat{i}$ for $\Delta f = \frac{m}{2\tau}$ to $\pi(\frac{\hat{i}}{\sqrt{2}} + \frac{\hat{k}}{\sqrt{2}})$ for $\Delta f = \frac{1}{4\tau} + \frac{m}{2\tau}$. The latter results in $\tilde{\varrho}$ experiencing antiresonant kicking as it alternates between the ij plane and the k axis between echoes. This can produce a rapidly oscillating initial signal, such as that shown in Fig. 2, since $\mathrm{Tr}[I_3^{W,V} I_{1,2}^{W,V}] = 0$.

The evolution of the signal under D and P for a given net rotation is performed numerically, but under certain conditions, namely, $\hat{n}_{\rm tot} = \hat{i}$, an analytical solution readily is available.[14] We briefly review this solution here and characterize the average echo response for a large number of echoes.

The signal for the nth echo, detected by the same coil that provided the excitation pulses, is

$$\langle \mathbf{I} \rangle \cdot \hat{B} = \hat{y} \cdot \hat{B} \langle I_y \rangle = \frac{2\hbar\omega_y}{3kT} \cos\psi \sin\omega_{rf} t \sin\theta_0 \left[\frac{2}{3} g^W + \frac{1}{3} g^V\right], \quad (20)$$

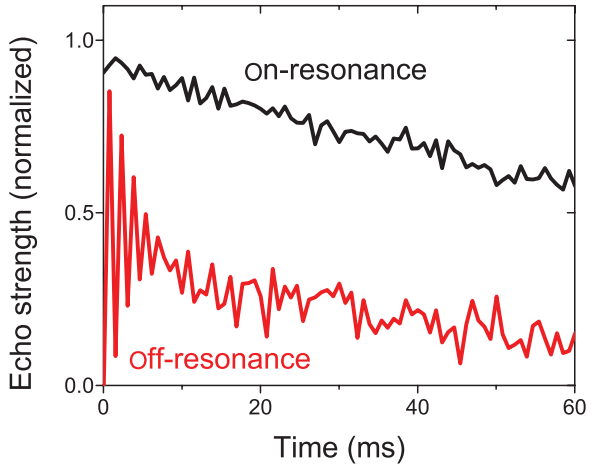

FIG. 2. (Color online) The signal from a 90-90 SLSE sequence is shown for both on-resonance ($\Delta f = 0$) and off-resonance ($\Delta f = \frac{1}{4\tau+2t_p}$) conditions. The heavy oscillations in the off-resonance signal are due to the large $\hat{k}$ component of $\hat{n}_{\rm tot}$ causing $\tilde{\varrho}$ to oscillate between the ij plane and the k axis. Data were taken at ω_y with $\tau = 335$ μs and $t_p = 100$ μs with the narrow sample described in Sec. III. Data here and elsewhere have been normalized to the amplitude of the $\Delta f = 0$ signal at $t = 0$.

where

$$g^i = 1 - 2F^i \sin^2 nx^i, \quad (21)$$

$x^i = \cos^{-1}[\cos\theta^i \cos d^i]$, $F^i = \frac{\cos^2\theta^i \sin^2 d^i}{1-\cos^2\theta^i \cos^2 d^i}$, and θ^i for the W and V levels is $\theta^W = \theta_{\rm tot}$ and $\theta^V = \frac{\theta_{\rm tot}}{2}$. Likewise, d^i, the angle of the rotation due to dipolar coupling evolution, varies between the W and the V levels $d^W = \alpha_y\tau$ and $d^V = (\alpha_z - \alpha_x)\tau$. Focusing on the W levels that provide two thirds of the signal, we can drop the superscripts. Using the standard sum for $\sin^2 nx$,[21] the average signal over a number of echoes N is proportional to the average value of g,

$$\bar{g} = 1 - \left(1 - \frac{\cos[(N+1)x]\sin Nx}{N \sin x}\right) F, \quad (22)$$

which reduces to

$$\bar{g} \approx 1 - F \quad (23)$$

for large N and $d \ll 1$. The restriction on the size of d follows from the need to keep τ small enough for the signal to be well refocused. For $\theta_{\rm tot} = m\pi$, $F = 1$ and the average signal will disappear. However, for $\theta_{\rm tot} = (2m+1)\frac{\pi}{2}$, the average signal will go to a maximum as $\bar{g} = 1$. This corresponds to the full refocusing of the dipolar coupling evolution. We note that, for the V levels, the signal disappears for $\theta_{\rm tot} = 2m\pi$ and goes to a maximum for $\theta_{\rm tot} = (2m+1)\pi$. Therefore, for $\theta_{\rm tot} = \pi$, the signal from the V levels will be refocused, while the signal from the W levels will decay.

The sensitivity of the loss of signal for $\theta_{\rm tot} = \pi$ is found by expanding $\theta_{\rm tot}$ as $\pi + \Delta\theta$ where $\Delta\theta$ is considered a perturbation. This allows F to be approximated as

$$F \approx \frac{d^2}{\Delta\theta^2 + d^2}, \quad (24)$$

which provides a simple relationship relating the expected size of the signal due to the dipolar coupling decay to $\Delta\theta$ and the size of d,

$$\Delta\theta^2 = \left(\frac{\bar{g}}{1-\bar{g}}\right) d^2. \quad (25)$$

This says that, for the signal to be half the maximum, $\Delta\theta$ and d should be equal.

We conclude that the dipolar coupling decay in the W levels should clearly be observable in two thirds of the signal when

$$\theta_{\rm tot} = \pi \pm d \quad \text{and} \quad \hat{n}_{\rm tot} = \hat{i}. \quad (26)$$

These requirements define the 180° condition. While this is impossible to achieve for all crystallites in the powder, under certain conditions, namely, $\Delta f = \frac{1}{4\tau} \pm \frac{m}{2\tau}$, the constraint on $\theta_{\rm tot}$ can be met. We previously found, for this off-resonant condition with δ-function pulses, that $\theta_{\rm tot}\hat{n}_{\rm tot} = \pi(\sin\frac{\theta_2}{2}\hat{i} + \cos\frac{\theta_2}{2}\hat{k})$. Therefore, the net rotation will be π for the entire powder sample. The direction of $\hat{n}_{\rm tot}$ can be brought close to $\hat{i}$ by choosing the pulse strength such that a large portion of the signal producing spins experiences a θ_2 close to π. This corresponds to $\theta = 2 \times 2.077$. Under these conditions, we can expect to see a large decay. For those crystallites experiencing $\theta_2 \neq \pi$ so that $\hat{n}_{\rm tot} \neq \hat{i}$, the effect is to reduce the decay rate by $\sin^2(\frac{\theta_2}{2})$ as determined by numerical simulations. This effect is understood by looking at $\theta_2 = \frac{\pi}{2}$ where the signal only is

TABLE II. The predicted value of $\Delta\omega_W$, from Eq. (28), and also $T_d = \frac{1}{\sqrt{\langle\Delta\omega^2\rangle_W}}$ for both a single crystal and a powder under a 90-180 sequence. In calculating the second moment, all nitrogen within a sphere of radius $4d$, where d is the largest length of the unit cell, were considered.[15]

		Predicted values of T_d (ms)	
f_{NQR} (MHz)	$\frac{\sqrt{\langle\Delta\omega^2\rangle_W}}{2\pi}$ (Hz)	Single crystal	Powder
$\frac{\omega_x}{2\pi} = 4.64$	21	7.5	8.7
$\frac{\omega_y}{2\pi} = 3.60$	35	4.5	5.2
$\frac{\omega_z}{2\pi} = 1.04$	21	7.5	8.7

apparent every other echo because of the antiresonant kicking as demonstrated in Fig. 2. Since there is no evolution of the signal absent an echo, the decay rate is decreased by a factor of $\frac{1}{2}$. Looking at a powder, the apparent decay rate is predicted to be 86% of the value for the single-crystal result.

For nuclei a, the contribution to the second moment of its NQR signal due to each neighbor b comes from Vega,[8]

$$\langle\Delta\omega^2\rangle = \sum_b \frac{1}{3}\frac{\left(d_{ab}^V\right)^2}{\tau^2} + \frac{2}{3}\frac{\left(d_{ab}^W\right)^2}{\tau^2}. \tag{27}$$

Since our sequence refocuses the signal from the V levels, the observed decay in time is determined by the contribution of the W levels to the second moment,

$$\langle\Delta\omega^2\rangle_W = \sum_b \frac{2}{3}\frac{\left(d_{ab}^W\right)^2}{\tau^2}, \tag{28}$$

where

$$\sum_b \frac{\left(d_{ab}^W\right)^2}{\tau^2} = \sum_b \alpha_{y_{ab}}^2 \equiv \alpha_{y_{\mathrm{eff}}}^2. \tag{29}$$

The last line defines an effective dipolar coupling frequency $\alpha_{y_{\mathrm{eff}}}$ that takes the multispin nature of the system into account. Using calculations performed by Sauer and Klug for sodium nitrite,[15] the predicted width of the Gaussian component of the echo train T_d follows, with the results shown in Table II for both a single crystal and a powder.

III. EXPERIMENTAL PROCEDURE

Experiments were performed on two powder samples of sodium nitrite $NaNO_2$ encased in wax to reduce piezoelectric effects: a 32-g sample (97.1% purity) manufactured by Fisher Scientific in 1979 and a 27-g sample (99.5% purity, superfree flowing) manufactured by Sigma-Aldrich in 2005. Despite having a lower purity, the quarter century older sample had a narrower linewidth, measured with a free-induction decay (FID) signal obtained after a single-excitation pulse due to a smaller EFG inhomogeneity. This was because of the considerably larger crystallites of the sample as was demonstrated by grinding the narrow sample with a mortar and pestle and finding the linewidth was now comparable to the broader linewidth of the Sigma-Aldrich sample. We, therefore, call the Fisher Scientific sample the narrow sample and the Sigma-Aldrich sample the broad sample with their linewidths given in Table III. This variation in linewidth due to crystallite size explains, at least in part, the variation in linewidths reported in the literature for sodium nitrite at room temperature.[22–25] Another group has demonstrated a similar dependency of NQR linewidth on crystal size for other substances.[26]

All experiments were carried out at room temperature using a Tecmag-based spectrometer (Tecmag, Houston, TX). A homebuilt probe with a coil that encased the sample was used and was tuned to the various NQR frequencies. Unless stated otherwise, the quality factor $\mathcal{Q}$ was typically 20 or less, and the rf input power was 1000 W or less. As discussed in more detail in Sec. III B, the low-quality factor was chosen to create pulses that approached an idealized square pulse.

The experiments consisted of performing pulse sequences on each sample at various off-resonances. A typical trial consisted of $\geqslant 64$ scans at a given off-resonance in order to provide a useful signal-to-noise ratio (SNR). Before a trial, it was necessary to measure the exact NQR frequency with an FID to ensure that the correct off-resonance was used. After the NQR frequency was found, another FID was taken at $\Delta f = 0$, and the signal was backprojected to find its magnitude at $t = 0$. This value provided the normalization coefficients of the SLSE signals that were used in the figures.

Two types of pulse sequences were used. The 90-90 SLSEs consisted of an optimal excitation pulse $\theta_0 = 2.077$ corresponding to a $\frac{\pi}{2}$ pulse for a powder and refocusing pulses of the same strength. The second sequence, the 90-180, had the same excitation pulse as the 90-90, but with a refocusing pulse that produced twice the rotation $\theta = 4.154$ corresponding to a π pulse for a powder. Both the excitation and the refocusing pulses for all 90-90 sequences used pulse lengths of 100 μs with the same rf amplitude. For the 90-180 sequences, a fixed rf amplitude was used for each pulse, but the refocusing pulse was twice as long as the excitation pulse. For ω_x and ω_y, the excitation pulse was 50-μs long, while the ω_z experiments

TABLE III. The observed full width at half maximum linewidths for both samples at the three NQR transition frequencies show that the broad sample has a larger linewidth for all three frequencies. The EFG component is found by decomposing the linewidth's Voigt profile into the predicted Gaussian (dipolar coupling) and Lorentzian (EFG) components. Measurements for all linewidths are accurate to within 20 Hz.

	Narrow sample		Broad sample	
f_{NQR}	Total width (Hz)	EFG component (Hz)	Total width (Hz)	EFG component (Hz)
ω_x	185	125	390	361
ω_y	154	97	309	280
ω_z	143	67	215	163

used 100-μs pulses due to limitations in the amplifier that required weaker pulses at the lower frequency. For δ-function pulses, the signal's off-resonance behavior is predicted to have a period of $\frac{1}{2\tau}$ as discussed above. For finite pulses, we observe experimentally that this periodicity is close to $\frac{1}{2\tau+tp} \equiv \frac{1}{2\tau'}$, particularly for the 90-90 sequences. For this reason, our experimental graphs, where the rf frequency is varied, are expressed in terms of $\Delta f\ \tau'$. For the ω_x and ω_y transitions, data were taken between $\pm\frac{2}{\tau'}$. Due to the low SNR and electronics limitations, data for ω_z were only taken on-resonance and at $\Delta f = \pm\frac{1}{4\tau'}$.

A. Experimentally achieving the 180° condition for finite pulses

All observed echo trains were fit to the function

$$S(t) = A\left\{p_g \exp\left[-\frac{1}{2}\left(\frac{t}{T_d}\frac{\tau}{\tau'}\right)^2\right] + [1-p_g]\exp\left[\frac{-t}{T_{2e}}\right]\right\}, \tag{30}$$

where A is amplitude at $t = 0$, T_{2e} is the long-term decay constant, p_g is the percent of the signal due to the Gaussian decay, and T_d is the width of the Gaussian decay associated with the strength of the dipolar coupling. The addition of the $\frac{\tau}{\tau'}$ term to the Gaussian component is because there is no evolution due to the dipolar coupling during the finite pulse lengths.

The experimental conditions, with finite pulses, that lead to a strong Gaussian component were found using Eq. (18) and the limit $\theta_{\text{tot}} = \pi \pm d$ of the 180° condition. This led to the constraint that

$$\left|\cos\,\theta_1 \cos\frac{\theta_2}{2} - \sin\,\theta_1 \sin\frac{\theta_2}{2}\hat{n}_2\cdot\hat{k}\right| \leqslant \frac{d}{2}. \tag{31}$$

This equation must be satisfied for a large portion of the sample in order to see the rapid decay in the signal due to the dipolar coupling. But θ_1,θ_2, and $\hat{n}_2\cdot\hat{k} = \frac{\theta_1}{\theta_2}\frac{t_p}{\tau}$ all vary among nuclei due to the EFG inhomogeneity, while θ_2 and $\hat{n}_2\cdot\hat{k}$ also vary with the random alignment of the rf with respect to the crystallite's orientation. In order to satisfy the inequality, it is necessary to keep both the cosine ($\cos\,\theta_1 \cos\frac{\theta_2}{2}$) and the sine ($\sin\,\theta_1 \sin\frac{\theta_2}{2}\hat{n}_2\cdot\hat{k}$) terms small. The conditions that make this possible for a large portion of the sample determine the pulse and sample characteristics necessary to observe the decay due to dipolar coupling.

The sine term is small for all crystallites when

$$|\hat{n}_2\cdot\hat{k}| \leqslant \frac{d}{2}, \tag{32}$$

which is easily met when the value of $\frac{t_p}{\tau} \ll 1$. The cosine term is small for all crystallites when $|\cos\,\theta_1| \leqslant \frac{d}{2}$. If Δf represents the average off-resonance, then $\theta_1 = 2\pi(\Delta f + \delta f_{\text{EFG}})\tau$ where δf_{EFG} is a nuclei's additional off-resonance due to EFG inhomogeneity. The cosine inequality fully is satisfied when $\Delta f = \frac{1}{4\tau} + \frac{m}{2\tau}$ and $2\pi\ \delta f_{\text{EFG}} \leqslant \frac{\alpha_{y_{\text{eff}}}}{2}$. This shows that the 180° condition is met for a majority of the sample when the linewidth broadening due to EFG inhomogeneity is less than or equal to that due to W-level dipolar coupling. This condition is unnecessarily strict for pulse strengths where $\theta_2 \approx \pi$, corresponding to a 90-180 sequence as shown experimentally with a sample where the linewidth broadening clearly is dominated by EFG inhomogeneity.

In addition to the requirement that θ_{tot} be close to π, the direction of the net rotation must be close to $\hat{i}$ in order to both avoid heavy oscillations and to accurately measure the dipolar coupling. Examining Eq. (19) under the assumption $\theta_{\text{tot}} = \pi$ reveals that $\hat{n}_{\text{tot}} \approx \hat{i}$ when $\theta_2 \approx \pi$ and $\hat{n}_2 \approx \hat{i}$. The latter condition can only be met when the rotation due to off-resonance during the pulse is kept small. This requires $\Delta f = \pm\frac{1}{4\tau}$ when τ is small, but allows $\Delta f = \frac{1}{4\tau} + \frac{m}{2\tau}$ as τ increases. Together, these constraints define the experimental conditions under which the strongest decay due to the dipolar coupling should appear, a 90-180 sequence and $\Delta f = \pm\frac{1}{4\tau}$. In addition to the frequency and strength of the pulse, the timing of the pulses must be chosen with respect to the duration in time of the pulses. Since the finite-pulse lengths can inhibit the decay, the minimum τ to operate at is derived from the requirement that $|\hat{n}_2\cdot\hat{k}| \leqslant \frac{d}{2}$. This leads to the relation $\tau^2_{\text{min}} \geqslant \frac{|\theta_1|}{\theta_2}\frac{2t_p}{\alpha_{y_{\text{eff}}}} \approx \frac{t_p}{\alpha_{y_{\text{eff}}}}$ for the 90-180, which is in good agreement with the experimental results shown in Sec. IV.

B. Effect of nonideal pulses

While the previous derivation would suggest covering all of the experimental parameters under which the 180° condition is met for a large portion of a sample, some preliminary experimental work suggests a more complex picture. When performing 90-180 sequences with a high $\mathcal{Q}(180)$ probe, we obtained asymmetric average signals, such as those shown in Fig. 3, most noticeably at the $\Delta f = \pm\frac{1}{4\tau'}$ conditions and for short values of τ. This asymmetry was never observed for any 90-90 sequence. Since achieving the 180° condition leads to a rapid decay in signal strength for the echo train, the asymmetric data imply that the percentage of signal from spins experiencing the 180° condition varies with the sign of the off-resonance.

To understand the asymmetry's source, the shapes of the actual refocusing pulses were used to model the behavior

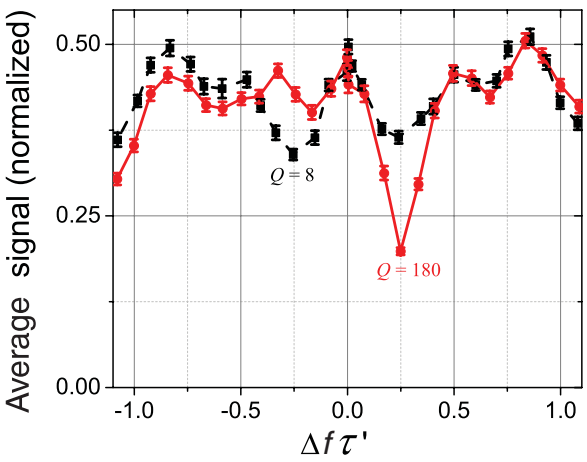

FIG. 3. (Color online) A plot of the average signal over 125 ms versus $\Delta f\ \tau'$ for fixed τ (335 μs) shows that the asymmetry between $\Delta f = \pm\frac{1}{4\tau'}$ was reduced by lowering the $\mathcal{Q}$ of the probe. Data were taken with a 90-180 sequence at ω_y with the broad linewidth sample and $t_p = 100$ μs.

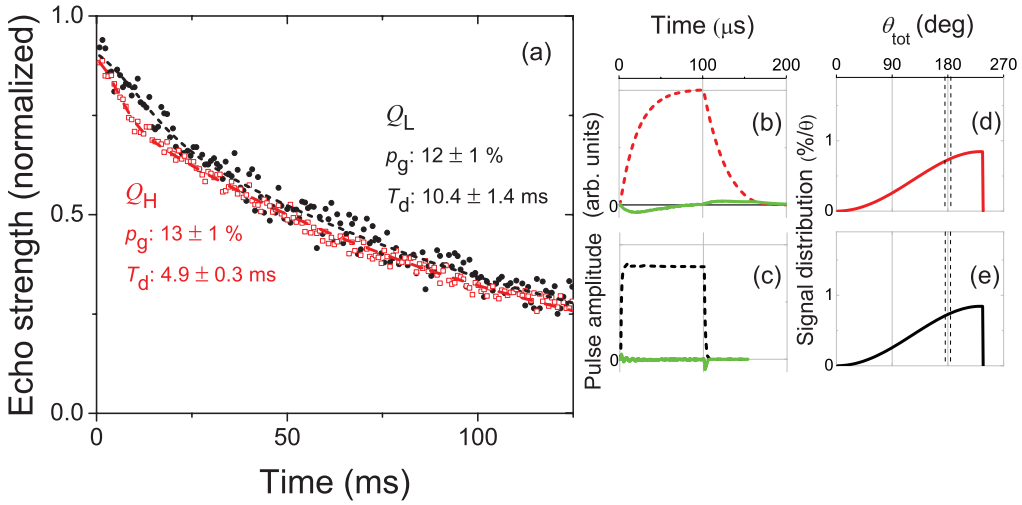

FIG. 4. (Color online) For $\Delta f = 0$, the (a) echo trains with high $\mathcal{Q}$ ($\mathcal{Q}_H$, hollow red squares) and low $\mathcal{Q}$ ($\mathcal{Q}_L$, black circles) are similar, despite their respective pulse shapes, (b) and (c), having very different real (dashed lines) and imaginary (green solid lines) components. This is understandable in view of the similarities of the calculated distributions of the initial signal as a function of θ_{tot} given in (d) and (e) for the pulse shapes to their left. The dashed black vertical lines correspond to the boundaries for $\theta_{\text{tot}} = \pi \pm d$ that determine the percentage p_{th} of the echo train due to a Gaussian component. This and the following data in this section are from a 90-180 sequence applied to the narrow sample at ω_y, $\tau = 335$ μs, and $t_p = 100$ μs.

of a powder during a SLSE sequence. The pulse shapes were obtained by measuring the strength of the magnetic field in the main coil with the voltage induced in a sniffer coil located several centimeters away. Using the model of Sec. II, the percent of the initial signal due to the spins experiencing an effective 180° rotation p_{th} was calculated with examples shown in Figs. 4 and 5. We found p_{th} perfectly rank ordered the normalized average signal size at the $\Delta f = \pm\frac{1}{4\tau'}$ condition across multiple configurations of the probe as shown in Fig. 6(a). Additionally, fitting the echo train revealed p_{th} roughly predicted the Gaussian contribution associated with the percentage of spins experiencing a 180° rotation as shown

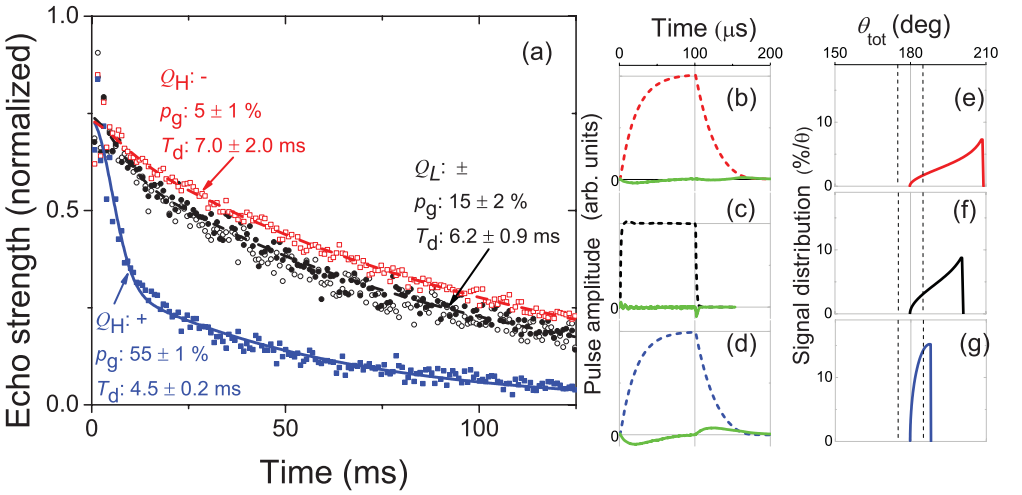

FIG. 5. (Color online) (Left) The (a) echo trains show that, for a high $\mathcal{Q}$ ($\mathcal{Q}_{\text{H}}$) probe, a strong Gaussian component appears at $\Delta f = +\frac{1}{4\tau'}$ (blue squares) whose width is somewhat below the prediction from Table II. This requires further investigation. This component was absent for $\Delta f = -\frac{1}{4\tau'}$ (hollow red squares) and for both low $\mathcal{Q}$ ($\mathcal{Q}_{\text{L}}$) trains at $\Delta f = +\frac{1}{4\tau'}$ (solid black circles) and $\Delta f = -\frac{1}{4\tau'}$ (hollow black circles). (Middle) Comparing pulse shapes, the (c) $\mathcal{Q}_{\text{L}}$ configuration has a different real (dashed lines) component compared to the $\mathcal{Q}_{\text{H}}$ configurations for both (b) $\Delta f = -\frac{1}{4\tau'}$ and (d) $\Delta f = +\frac{1}{4\tau'}$. Additionally, its small imaginary component (green solid lines) is less pronounced than both the $\mathcal{Q}_{\text{H}}$ $\Delta f = -\frac{1}{4\tau'}$ pulse and the $\mathcal{Q}_{\text{H}}$ $\Delta f = +\frac{1}{4\tau'}$ pulse, which has a large imaginary component. (Right) Corresponding to each pulse, the distribution of the initial signal as a function of θ_{tot} was calculated. For the $\mathcal{Q}_{\text{L}}$ pulses, the distribution does not depend on the sign of Δf, which is why the echo trains for $\Delta f = -\frac{1}{4\tau'}$ and $\Delta f = +\frac{1}{4\tau'}$ are very similar. In comparison, for the $\mathcal{Q}_{\text{H}}$ pulses, the combination of the off-resonance and the nonzero imaginary component works to reduce the distribution near $\theta_{\text{tot}} = 180°$ for $\Delta f = -\frac{1}{4\tau'}$ while substantially increasing it for the $\Delta f = +\frac{1}{4\tau'}$ pulse distribution. For the former, the result is to reduce the strength of the observed Gaussian component compared to the $\mathcal{Q}_{\text{L}}$ trains. In the latter, the combination leads to the very strong decay.

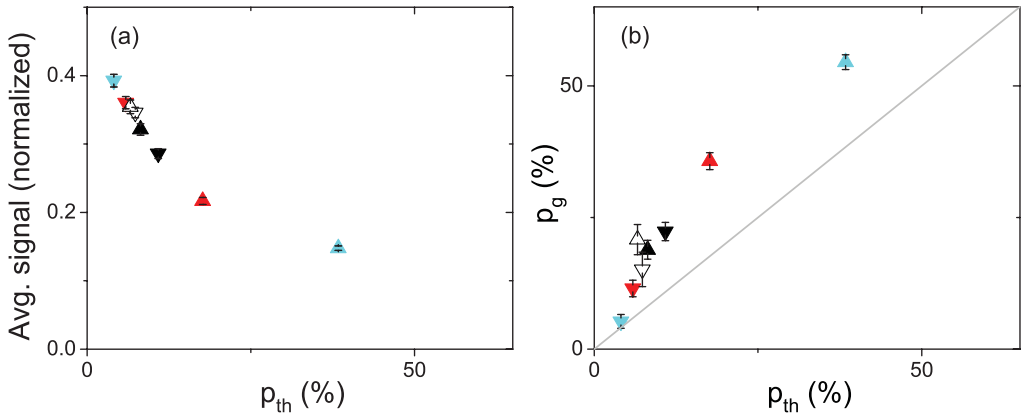

FIG. 6. (Color online) (a) Average signal and strength of the Gaussian contribution of the (b) echo train versus p_{th}, the calculated percent of the initial signal due to spins experiencing a 180° net rotation. For both values, p_{th} does an excellent job rank ordering, validating the significance of the 180° condition to the behavior of the echo train. The data come from several probe configurations. With a high $\mathcal{Q}$ (180), the probe was tuned to f_{NQR} (red), $f_{\mathrm{NQR}} + \frac{1}{4\tau'}$ (cyan), and $f_{\mathrm{NQR}} - \frac{1}{4\tau'}$ (black). The hollow black data are at low $\mathcal{Q}$ (8) with the probe tuned to f_{NQR}. Data taken at $\Delta f = \frac{1}{4\tau'}$ are indicated by the upward triangles; $\Delta f = -\frac{1}{4\tau'}$, downward triangles. Data were taken over 125 ms.

in Fig. 6(b). These results confirmed that the asymmetry of the average signal was due to variations in the distribution of spins experiencing the 180° rotation as a function of the pulse shape.

By setting the imaginary component of the actual pulses to 0, the model produced symmetrical distributions of θ_{tot} for the high $\mathcal{Q}$ pulses at $\Delta f = \pm\frac{1}{4\tau'}$; these also conformed to the distributions from the low $\mathcal{Q}$ pulses at $\Delta f = \pm\frac{1}{4\tau'}$. To see how the presence of a nonzero imaginary component could produce the asymmetric distributions, a fake pulse, shown in Fig. 7, was created that roughly mimicked the real pulse.

The net rotation due to this fake pulse at $\Delta f = \pm\frac{1}{4\tau'}$, i.e., the point of the major asymmetry in the data, was found by breaking the pulse into two nearly identical rotations, $\theta_a\hat{n}_a$ and $\theta_b\hat{n}_b$ differing only in the sign of their imaginary components,

$$\hat{n}_a = \frac{R\hat{\imath} - I\hat{\jmath} + F\hat{k}}{\theta_a}, \qquad \hat{n}_b = \frac{R\hat{\imath} + I\hat{\jmath} + F\hat{k}}{\theta_a}, \tag{33}$$

$$\theta_a = \theta_b = \sqrt{R^2 + I^2 + F^2}, \tag{34}$$

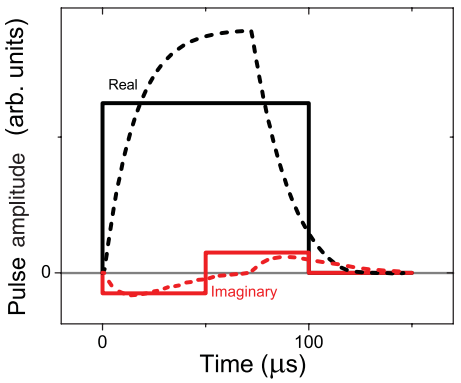

FIG. 7. (Color online) The real (black) and imaginary (red) components of an actual (dashed lines) and simplified (solid lines) refocusing pulse shape. The latter is useful for understanding the significance of the imaginary component to achieve the 180° condition.

where $F = \theta_1\frac{t_p}{\tau}$. Using quaternions to combine $\theta_a\hat{n}_a$ and $\theta_b\hat{n}_b$ as a single rotation $\theta_2\hat{n}_2$ (Refs. 27 and 28) reveals $\hat{n}_2 \cdot \hat{k} = 0$, making $\theta_{\mathrm{tot}} = \pi$ via Eq. (18), when

$$F\cos\frac{\theta_a}{2} = \frac{RI}{\theta_a}\sin\frac{\theta_a}{2}. \tag{35}$$

With a nonzero imaginary component, Eq. (35) can only be satisfied for one sign of the off-resonance. This explains many observed phenomena. It explains the origin of the asymmetry, because the 180° condition now depends on the sign of the off-resonance. It explains why dropping the $\mathcal{Q}$ reduced the asymmetry because it forced the imaginary component to zero. And finally, it explains why the asymmetry was reduced with τ: as τ increases, F approaches 0, and Eq. (35) no longer is satisfied for either sign of off-resonance.

IV. EXPERIMENTAL RESULTS

Examples of theoretical and actual signal behavior for various experimental parameters are shown in Fig. 8 for the narrow sample at frequencies close to ω_y. Since the model does not include the long-term T_{2e} effects, its accuracy is limited in the long-term behavior for both sequences. For this reason, we compare the initial signal to theoretical calculations that have been scaled to match the data. The rapidly alternating initial signal near $\Delta f = \frac{1}{4\tau'} + \frac{m}{2\tau'}$ for the 90-90's due to the antiresonant kicking is captured by the model. Additionally, the conditions where dipolar coupling is not refocused for a large portion of the sample are seen in the undulating signal of the 90-180's near the $\Delta f = \frac{1}{4\tau'} + \frac{m}{2\tau'}$ locations. The period of the undulations depends on the second moment in Table II and is given as $\frac{2\pi}{\alpha_{y_{\mathrm{eff}}}}\frac{\tau'}{\tau}$. For small τ, these undulations are weak as the finite pulses prevent a large portion of the sample from experiencing the 180° condition. For larger τ, as the ratio of t_p to τ makes the pulses appear more like δ-functions, the oscillations become more apparent as expected. These undulations are not observed in the corresponding actual signals since they manifest themselves as a Gaussian decay

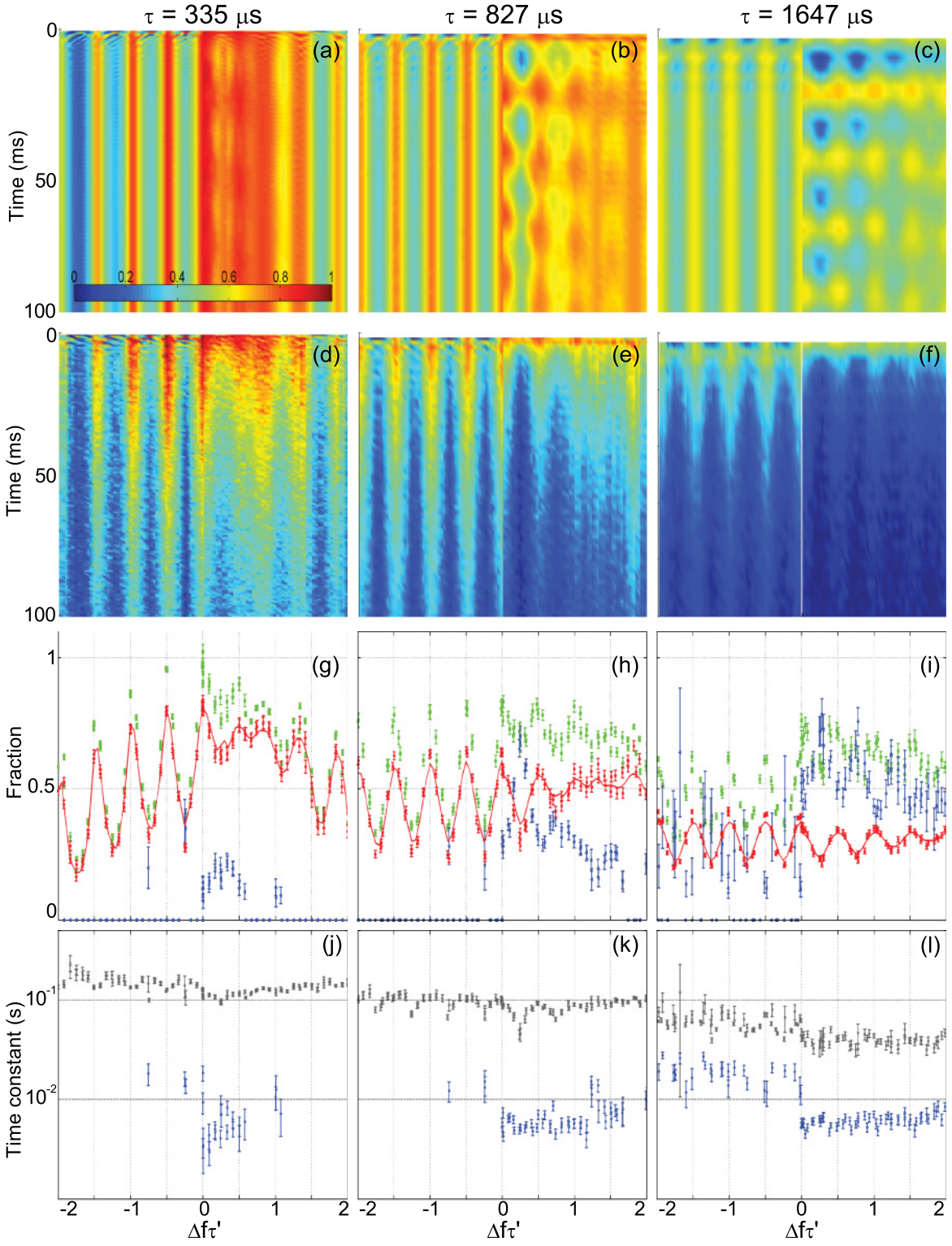

FIG. 8. (Color online) The (a)–(c) theoretical and (d)–(f) experimental data are compared with off-resonance for both 90-90 and 90-180 sequences, the left and right halves of each image, respectively, for three values of τ. The model for a powder with finite pulses is from Sec. II. The fit parameters A (green squares) and p_g (blue triangles) of the observed signal, the average echo (red circles) over the $\frac{2\pi}{\alpha_{y_{\text{eff}}}}\frac{\tau'}{\tau}$ period of the dipolar coupling for ω_y, and the predicted average echo (red lines) are given in (g)–(i). The fit parameters T_{2e} (gray diamonds) and T_d (blue circles) are given in (j)–(l).

in the signal due to the variations in the phasing of the signals from the interaction of a large number of nuclei, as opposed to just a pair, as is modeled.

While not shown in Fig. 8, all of the experimental data were symmetrical as a function of off-resonance as predicted for a low Q probe. The 90-90 signals were periodic as a function

of off-resonance in excellent agreement with the model. The peaks correspond to $\Delta f = \frac{m}{2\tau'}$ where the magnetization is locked along the $\hat{i}$ direction and the troughs to $\Delta f = \frac{1}{4\tau'} + \frac{m}{2\tau'}$ where the signal is lost due to the antiresonant kicking. By increasing τ, the sharpness of the oscillations is reduced since the linewidth of the sample begins to approach $\frac{1}{4\tau'}$. As this condition is met, the signal is no longer dominated by either the on- or the off-resonance effects but by a mixture of the two. Similarly, the larger EFG component of the broad sample reduces the variation in signal behavior with frequency compared to the narrow sample for the same experiments.

The 90-180 data, again agreeing well with the model, show a similar periodicity as the 90-90 data in off-resonant behavior but with notable differences. For instance, while having roughly the same period, the local maxima and minima are not all at the $\Delta f = \frac{m}{4\tau'}$ conditions. This is because strong dips in the average signal are not primarily due to signal lost to antiresonant kicking but to achieving the 180° condition. For low τ and small Δf, the dips are fairly small because the 180° condition is hard to achieve at low τ with finite pulses. But as τ is increased, a strong decay is observed first at the $\Delta f = \pm\frac{1}{4\tau'}$ condition and then later at $\Delta f = \frac{1}{4\tau'} + \frac{m}{2\tau'}$ as expected.

Fitting the data to Eq. (30), it was found that A roughly tracked the average signal for all 90-90's. This was because there was no rapid decay in the echo train due to nuclei achieving the 180° condition. For the 90-180's, however, A tracked the average signal well for short τ but diverged for larger τ as the Gaussian component of the decay rapidly drove the average signal down. This is apparent at $\Delta f = \pm\frac{1}{4\tau'}$ for $\tau = 827\ \mu$s. As τ increased, the separation between A and the average echo became noticeable across all off-resonances as more of the signal experienced the 180° condition. This same explanation is used for the behavior of p_g for 90-180's. For low τ, p_g is close to zero since the 180° condition is met for only a small subset of spins. Then, as shown in Fig. 9, near the predicted value of $\tau_{\min}$ at $\Delta f = \pm\frac{1}{4\tau'}$, p_g becomes substantial as the 180° condition is met for a larger percentage of the sample, approaching the two-thirds value predicted by Eq. (20). As p_g plateaus for large τ, it becomes significant across the entire range of off-resonances as the EFG inhomogeneity ensures a significant fraction of the spins experience the 180° condition, regardless of the off-resonance of the pulses.

While Fig. 8 focuses on the narrow sample at ω_y, in Fig. 9, it is shown that similar behaviors for 90-180 sequences at $|\Delta f| = \frac{1}{4\tau'}$ appear across all three NQR frequencies, even for a sample with a much larger EFG contribution to its linewidth. In particular, the values of p_g for $|\Delta f| = \frac{1}{4\tau'}$ are consistently higher than for $\Delta f = 0$ since more of the sample experiences the 180° condition. This also explains why the narrow sample consistently has a larger p_g for $|\Delta f| = \frac{1}{4\tau'}$ than the broad sample but a smaller value for $\Delta f = 0$. Additionally, regardless of the contribution of the linewidth due to EFG inhomogeneity, p_g approaches a constant value for $|\Delta f| = \frac{1}{4\tau'}$ as τ increases. The value of $\tau_{\min}$, where this plateau is expected to arise, comes from the argument in Sec. III A and is marked by a vertical black line in Fig. 9. Beyond $\tau_{\min}$, the measurements of T_d converged, as shown in Figs. 8 and 9, regardless of the sample or the off-resonance of the pulses. For ω_x and ω_y, the converged values agree well with the theoretical values, after accounting for the effects of a powder sample. However, for both ω_y and ω_z, the converged value was slightly higher than expected. It is known that the NO_2 ion in sodium

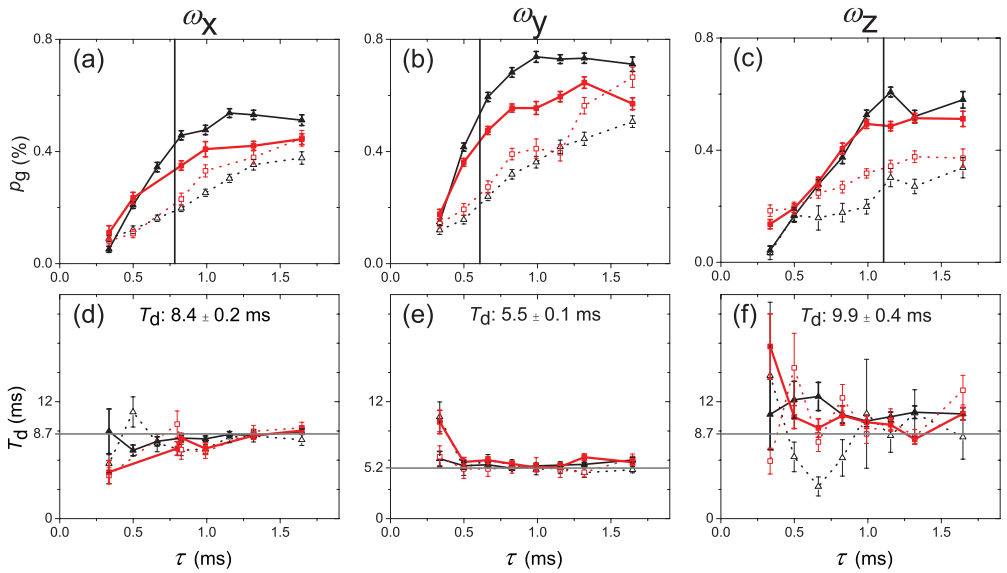

FIG. 9. (Color online) The percent of the decay in the echo train due to the (a)–(c) Gaussian component p_g and (d)–(f) width of the Gaussian contribution T_d as a function of τ for 90-180 sequences applied at the three transition frequencies. Values were obtained by fitting the echo trains of 90-180 sequences with Eq. (30). Measurements were made for both the narrow (black triangles) and the broad (red squares) samples for $|\Delta f| = \frac{1}{4\tau'}$ (solid lines, symbols) and $\Delta f = 0$ (dashed lines, hollow symbols). The vertical line marks $\tau_{\min}$, the theoretical minimum τ to observe a strong decay due to the dipolar coupling at $|\Delta f| = \frac{1}{4\tau'}$. This prediction does not depend on EFG inhomogeneity, as is experimentally validated, since the plateau for the narrow sample matches that of the broad sample. Additionally, the predicted value accurately accounts for the impact of doubling the refocusing pulse length needed to perform the ω_z experiments. The measurements of T_d converge, regardless of the EFG inhomogeneity of the sample, close to the predicted values (gray lines). The average T_d, for $\tau > \tau_{\min}$ and $\Delta f = 0, \pm\frac{1}{4\tau'}$, is given at the top of (d)–(f).

nitrite exhibits rapid torsional oscillation about the x axis of the PAF.[29] This would result in a reduction in the dipolar coupling strength for the ω_y and ω_z transitions.

As shown in Fig. 8, for the 90-90's, there were very few off-resonance conditions at low τ that led to a significant Gaussian contribution to the echo train since only a small portion of the nuclei experience the 180° condition. As τ increased and the behavior of the signal became more uniform with frequency, T_d converged to a fixed value that was three times longer than the single crystal's value. A naive theoretical adjustment that ignores both the EFG inhomogeneity and the powder average also predicts a lengthening of T_d but only by a factor of 2.

For a given τ, the measurements of T_{2e} varied by a factor of 3 within the range of off-resonances tested, a result comparable to the variations observed by Gregorovic *et al.* using PNT.[9] However, in general we observed longer T_{2e}'s for $\Delta f = \frac{m}{2\tau'}$ than for $\Delta f = \frac{1}{4\tau'} + \frac{m}{2\tau'}$, in contrast to Gregorovic *et al.*, perhaps due to their focus on the long-time echo data and short τ. Our general trend in T_{2e}, as a function of τ, was the same for all transition frequencies and is shown for ω_y in Fig. 10. While our simple model does not predict the long-time behavior, T_{2e} does seem correlated with the short-time behavior caused by the 180° condition and antiresonant kicking. For example, the 90-90 sequence at $\Delta f = 0$ predominantly produced a longer T_{2e} than the other sequences for the same τ in correspondence with the refocusing the W levels. This is in contrast to the 90-180 sequence where the W levels are not refocused and there is less signal due to achieving the 180° condition, particularly for $|\Delta f| = \frac{1}{4\tau'}$ and the narrow sample. Additionally, for the 90-90 at $|\Delta f| = \frac{1}{4\tau'}$, the antiresonant kicking causes a reduction in the initial signal.

The dependency of T_{2e} on τ was found by fitting the T_{2e} values for each sequence to the equation,

$$T_{2e}(\tau) = T_{2e}(\tau = 400\ \mu\text{s}) \left(\frac{\tau}{400\ \mu\text{s}} \right)^{-x}. \qquad (36)$$

The fit parameters of Table IV show that $T_{2e} \propto \tau^{-x}$ with $0.18 \leqslant x \leqslant 0.61$. While this is in contrast to the τ^{-5} dependency observed by Marino and Klainer,[6] who operated at 77 K, a weaker dependency has been observed by Mikhaltsevitch and Rudakov at room temperature.[10] Additional work with sodium nitrite at 77 K suggests a more complex dependency between T_{2e} and τ.[2] Interestingly, it was found that the values of $T_{2e}(\tau = 400\ \mu\text{s})$ decreased linearly with f_{NQR} for the on-resonant sequences.

For the real-world detection of illicit substances using NQR, the exact resonance frequency of the sample may only be known to within a certain range. This is due to the variation of the NQR frequencies with temperature, which can be several hundred hertz per degree for a substance such as RDX (cyclotrimethylenetrinitramine).[30] To prevent false negatives, a detector operator would want to know that a useful signal can be detected at all frequencies within that range. To compare the sequences as functions of off-resonance, an optimal SNR was calculated by integrating Eq. (30) over the time found to maximize the SNR with the results shown in Fig. 11. This allows us to define a useful signal as one achieving some minimum SNR. For short τ, the minimum possible SNR for the 90-90 sequence, over the given off-resonance domain, is considerably less than the minimum possible SNR of the 90-180 sequence, for both the narrow and the broad samples. This is because the 90-90 sequence triggers a larger loss of signal due to antiresonant kicking compared to that lost due to the 180° condition, which is inhibited at low τ due to finite pulses for the 90-180. For the intermediate τ, the two sequences share the same minimum SNR for the narrow sample, as the signal lost to the 180° condition and the antiresonant kicking become comparable between sequences. However, the 90-90 sequence is now slightly preferable for the broad sample at this intermediate τ. This shows that the optimal detection sequence for a given τ is a function of the relative strengths of the two dominant line-broadening mechanisms. Finally, we note that, at high τ, the 90-90 sequence is stronger for both samples with considerably less variation in amplitude with frequency for the broad sample due to its larger EFG inhomogeneity.

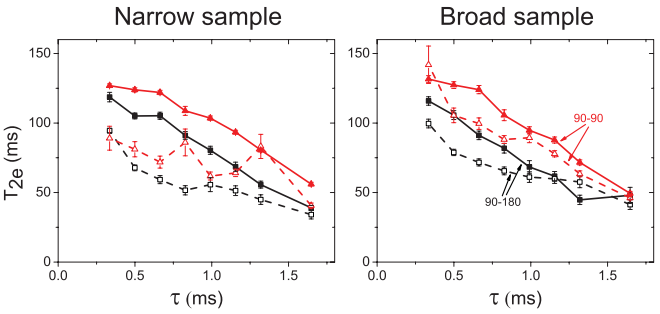

FIG. 10. (Color online) The value of T_{2e} for 90-180 (black squares) and 90-90 (red triangles) sequences is consistently greater when $\Delta f = 0$ (solid line and symbols) than for $|\Delta f| = \frac{1}{4\tau'}$ (dashed line and hollow symbols). The 90-90's consistently produce longer T_{2e}'s than 90-180's at the same off-resonance condition. For long τ, both sequences on- and off-resonance measurements converge as the distinction between on- and off-resonance signals disappears due to the EFG inhomogeneity. This also explains why the data for the broad sample show less variation between $\Delta f = 0$ and $|\Delta f| = \frac{1}{4\tau'}$. Data are from the ω_y transition.

TABLE IV. The τ dependency of T_{2e} was found by fitting the observed values of T_{2e} at each τ value to Eq. (36) for $\Delta f = 0$ for both 90-180 and 90-90 SLSEs with the narrow sample.

	Narrow sample 90-180		Narrow sample 90-90	
	$T_{2e}(\tau = 400\ \mu\text{s})$ ms	x	$T_{2e}(\tau = 400\ \mu\text{s})$ ms	x
ω_x	83.3 ± 1.9	0.19 ± 0.03	96.5 ± 2.3	0.18 ± 0.03
ω_y	121.4 ± 9.4	0.61 ± 0.11	128.8 ± 8.3	0.37 ± 0.08
ω_z	206.5 ± 9.1	0.30 ± 0.07	218.1 ± 8.4	0.33 ± 0.05

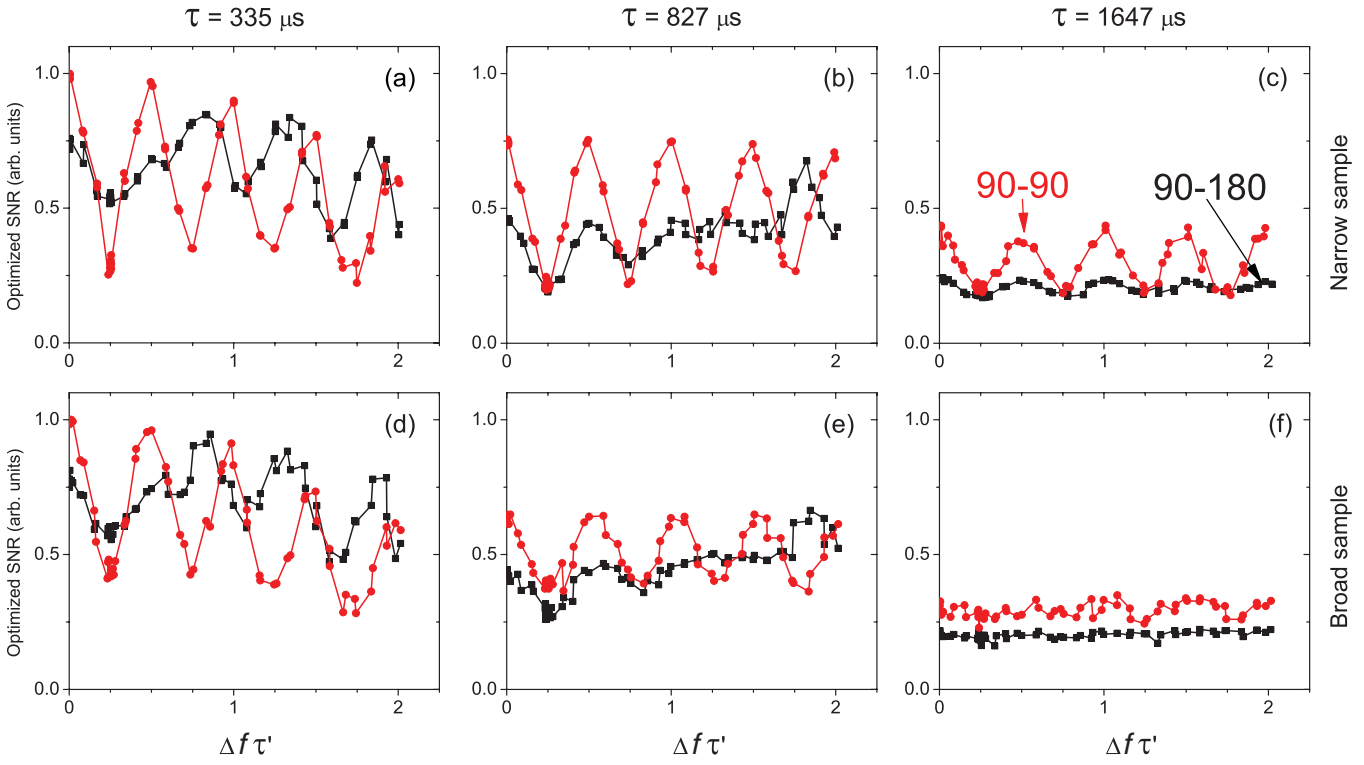

FIG. 11. (Color online) The optimal SNR calculated by integrating Eq. (30) for both 90-90 (red) and 90-180 (black) sequences with the experimentally derived fit parameters at ω_y for both the narrow (top row) and the broad (bottom row) samples. The integration was performed from $t = 0$ to the time that maximized the SNR. While finite pulses would reduce the amount of time that signal could be acquired, this adjustment is small and is not included. SNRs are normalized to the 90-90, $\Delta f = 0$, $\tau = 335$ μs, and $t_p = 100$ μs signals for each sample. The increased EFG inhomogeneity of the broad sample averages the variation between the maxima and the minima.

V. CONCLUSION

Despite the naive simplicity of the two-spin model, we have shown that it still qualitatively predicts the short-time behavior of the spin-locked signal as a function of off-resonance. Furthermore, the model permits us to identify the conditions under which we would expect a significant fraction of the signal to exhibit decay due to dipolar coupling alone. Namely, when the 180° condition is met for a large portion of the sample, the NQR signal experiences a rapid initial decay. To achieve this for a powder sample, one should operate with a 90-180 sequence, with an off-resonance $\Delta f = \pm\frac{1}{4\tau'}$, and with pulse spacing governed by $\tau \geqslant \sqrt{\frac{t_p}{\alpha_{y_{\text{eff}}}}}$. We have shown that operating with these conditions initially produces a Gaussian decay whose width measures the dipolar coupling between the nitrogen nuclei as shown in $NaNO_2$. Our measurements agree within 15% of the theoretical prediction after accounting for the powder nature of the sodium nitrite samples, and we believe that motion may account for part of the deviations in the experimental values from the theoretical values. Successfully performed for the three transition frequencies, this is a robust measurement that does not vary with the EFG inhomogeneity of our samples, nor does it require an exact π pulse across the sample as required in NMR.

For the purposes of substance detection, achieving the 180° condition for a large portion of the sample is to be avoided since it reduces the observed signal. However, the same conditions that can trigger the Gaussian decay also can trigger a loss of signal due to the antiresonant kicking with a 90-90 sequence. By knowing the strength of the dipolar coupling relative to the measured linewidth, it is possible to choose between these sequences to minimize the losses from their off-resonance effects. For substances where the dipolar coupling is unknown, this is not a problem. By simply running 90-180 sequences at $\Delta f = \pm\frac{1}{4\tau'}$ with ever increasing τ, the dipolar coupling eventually should reveal itself, allowing an accurate measurement to be made.

For short τ, the 180° condition is suppressed for 90-180 sequences at $\Delta f = \pm\frac{1}{4\tau'}$ due to the large value of the ratio of the pulse length to τ. This is beneficial for substance detection. However, we found that refocusing pulses with a definite imaginary component can overcome this constraint. The sensitivity of the signal to the sign of the imaginary component also allows the 180° condition to be suppressed for these sequences. This suggests further work with composite pulses designed to control off-resonant behavior by either suppressing or revealing evolution due to homonuclear dipolar coupling.

ACKNOWLEDGMENTS

We wish to thank Ted Lippert for his preparation of the sodium nitrite samples. This work was supported by NSF Grant No. 0547987.

*ksauer@physics.gmu.edu

[1]D. Y. Osokin, Phys. Status Solidi B **102**, 681 (1980).
[2]D. Y. Osokin, J. Mol. Struct. **83**, 243 (1982).
[3]O. S. Zueva and A. R. Kessel, J. Mol. Struct. **83**, 383 (1982).
[4]V. T. Mikhaltsevitch and T. N. Rudakov, Solid State Nucl. Magn. Reson. **25**, 99 (2004).
[5]M. M. Maricq, Phys. Rev. B **33**, 4501 (1986).
[6]R. A. Marino and S. M. Klainer, J. Chem. Phys. **67**, 3388 (1977).
[7]E. D. Ostroff and J. S. Waugh, Phys. Rev. Lett. **16**, 1097 (1966).
[8]S. Vega, Adv. Magn. Reson. **6**, 259 (1973).
[9]A. Gregorovic and T. Apih, J. Chem. Phys. **129**, 214504 (2008).
[10]V. T. Mikhaltsevitch and T. N. Rudakov, Phys. Status Solidi B **241**, 411 (2004).
[11]M. Engelsberg and C. S. Yannoni, J. Magn. Reson. **88**, 393 (1990).
[12]M. J. Lizak, T. Gullion, and M. S. Conradi, J. Magn. Reson. **91**, 254 (1991).
[13]T. Gullion, D. B. Baker, and M. S. Conradi, J. Magn. Reson. **89**, 479 (1990).
[14]R. S. Cantor and J. Waugh, J. Chem. Phys. **73**, 1054 (1980).
[15]K. L. Sauer and C. A. Klug, Phys. Rev. B **74**, 174410 (2006).
[16]A. Abragam, *The Principles of Nuclear Magnetism*, 2nd ed. (Clarendon, Oxford, 1961).
[17]C. P. Slichter, *Principles of Magnetic Resonance*, 3rd ed. (Springer, New York, 1996).
[18]E. W. Weisstein, *Dirac Matrices* [http://mathworld.wolfram.com/DiracMatrices.html] (Wolfram Research, Inc., Champaign, IL, 2011).
[19]S. Vega, J. Chem. Phys. **61**, 1093 (1974).
[20]T. N. Rudakov, V. T. Mikhaltsevich, and O. P. Selchikhin, J. Phys. D **30**, 1377 (1997).
[21]I. S. Gradshteyn and I. M. Ryzhik, *Table of Integrals Series and Products*, 4th ed. (Academic, New York, 1965).
[22]G. Petersen and P. J. Bray, J. Chem. Phys. **64**, 522 (1976).
[23]K. L. Sauer, B. H. Suits, A. N. Garroway, and J. B. Miller, J. Chem. Phys. **118**, 5071 (2003).
[24]P. K. Kadaba, D. E. O'Reilly, and R. Blinc, Phys. Status Solidi **42**, 855 (1970).
[25]S. K. Song *et al.*, J. Korean Phys. Soc. **36**, 287 (2000).
[26]M. L. Buess and S. L. Caulder, Appl. Magn. Reson. **25**, 383 (2004),
[27]K. L. Sauer, C. A. Klug, J. B. Miller, and A. N. Garroway, Appl. Magn. Reson. **25**, 485 (2004),
[28]M. H. Levitt, Prog. Nucl. Magn. Reson. Spectrosc. **18**, 61 (1986).
[29]R. Ambrosetti, R. Angelone, A. Colligiani, and A. Rigamonti, Phys. Rev. B **15**, 4318 (1977).
[30]R. J. Karpowicz and T. B. Brill, J. Phys. Chem. **87**, 2109 (1983).